LETTER

https://doi.org/10.1038/s41586-019-1247-7

Elastic colloidal monopoles and reconfigurable self-assembly in liquid crystals

Ye Yuan[1], Qingkun Liu[1], Bohdan Senyuk[1] & Ivan I. Smalyukh[1,2,3,4]*

Monopole-like electrostatic interactions are ubiquitous in biology[1] and condensed matter[2–4], but they are often screened by counter-ions and cannot be switched from attractive to repulsive. In colloidal science, where the main goal is to develop colloidal particles[2,3] that mimic and exceed the diversity and length scales of atomic and molecular assembly, electrostatically charged particles cannot change the sign of their surface charge or transform from monopoles to higher-order multipoles[4]. In liquid-crystal colloids[5–7], elastic interactions between particles arise to minimize the free energy associated with elastic distortions in the long-range alignment of rod-like molecules around the particles[5]. In dipolar[6,8], quadrupolar[8–12] and hexadecapolar[13] nematic colloids, the symmetries of such elastic distortions mimic both electrostatic multipoles[14] and the outermost occupied electron shells of atoms[7,15,16]. Electric and magnetic switching[17,18], spontaneous transformations[19] and optical control[20] of elastic multipoles, as well as their interactions with topological defects and surface boundary conditions, have been demonstrated in such colloids[21–23]. However, it has long been understood[5,24] that elastic monopoles should relax to uniform or higher-order multipole states because of the elastic torques that they induce[5,7]. Here we develop nematic colloids with strong elastic monopole moments and with elastic torques balanced by the optical torques induced by ambient light. We demonstrate the monopole-to-quadrupole reconfiguration of these colloidal particles by unstructured light, which resembles the driving of atoms between the ground state and various excited states. We show that the sign of the elastic monopoles can be switched, and that like-charged monopoles attract whereas oppositely charged ones repel, unlike in electrostatics[14]. We also demonstrate the out-of-equilibrium dynamic assembly of these colloidal particles. This diverse and surprising behaviour is explained using a model that considers the balance of the optical and elastic torques that are responsible for the excited-state elastic monopoles and may lead to light-powered active-matter systems and self-assembled nanomachines.

Microfabricated thin silica particles shaped as hexagonal prisms were surface-functionalized with azobenzene dye molecules to form molecular surface monolayers[25–27] (Extended Data Fig. 1). When dispersed in a nematic liquid crystal (LC)[4], such particles distort the alignment field of rod-like molecules (the nonpolar director field $\boldsymbol{n}(\boldsymbol{r}) \equiv -\boldsymbol{n}(\boldsymbol{r})$ with head–tail symmetry[5]) owing to the anisotropic interaction of the LC molecules with the surfaces of the colloidal particles[7] (Fig. 1). The particle-induced elastic distortions are manifested as spatial patterns of transmitted light intensity and colour when the LC colloidal sample is placed between polarizers and observed in an optical microscope using monochromatic (Fig. 1a, b) or white (Fig. 1i, j, l) light. Unlike conventional LC colloids, for which control of $\boldsymbol{n}(\boldsymbol{r})$ structures around particles requires high-power focused laser beams of optical tweezers[20], our photo-responsive nematic colloids exhibit polarizing optical microscopy textures and director structures highly dependent on the intensity, colour and polarization of low-intensity light, including microscope and ambient light (Fig. 1). Such facile reconfiguration of $\boldsymbol{n}(\boldsymbol{r})$ structures emerges from the collective reorientation of the azobenzene moieties[25–27] within monolayers on the surface of particles when they are exposed to light, which alters the molecular interactions at LC–colloidal interfaces, often causing rotation of particles and twisting of $\boldsymbol{n}(\boldsymbol{r})$ around them with respect to the uniform far-field director $\boldsymbol{n}_0$.

When observed with a conventional optical microscope, the particles appear to have a vector connecting two diametrically opposite vertices of the hexagonal facet of the colloidal platelet rotated with respect to $\boldsymbol{n}_0$ to an angle of $|\theta| < 30°$. For each particle, the sense of the rotation is random for unpolarized light or light with linear polarization along $\boldsymbol{n}_0$ (Fig. 1a–k) because of spontaneous symmetry breaking, but it can be controllably selected by slightly rotating the linear polarization direction away from $\boldsymbol{n}_0$. When rotated to the maximum angle θ above and below the platelet, $\boldsymbol{n}(\boldsymbol{r})$ smoothly twists back to uniform alignment with $\boldsymbol{n}_0$ far from the particle surfaces (Fig. 1g, h, Extended Data Fig. 1). Particles with opposite sense of $\boldsymbol{n}(\boldsymbol{r})$ rotation have different appearance when observed in both monochromatic (Fig. 1a, b) and white light (Fig. 1i, j), between polarizers with or without an additional phase-retardation plate in the optical pathway. To avoid spontaneous platelet rotation away from $\theta = 0°$, we can use red imaging light while carefully shielding the sample from ambient white light, or align the linear polarization of blue or achromatic light orthogonally to $\boldsymbol{n}_0$ (Fig. 1l, m, Extended Data Figs. 2, 3). This spectrally selective and polarization-dependent sensitivity of our colloids to light is consistent with the response of azobenzene dye molecules self-assembled on the particle surfaces[25–27].

Perturbations of $\boldsymbol{n}(\boldsymbol{r})$ away from $\boldsymbol{n}_0$ far from the rotated particles are monopole-like at $\theta \neq 0°$ (Fig. 1e, f, k), but become quadrupolar at $\theta = 0°$ (Fig. 1m). The twisted monopole-type director structure induced by a rotated platelet has low symmetry (Fig. 1g, k). By contrast, the quadrupolar structure has three mirror symmetry planes (Fig. 1l, m): one is orthogonal to both the platelet and $\boldsymbol{n}_0$, and two are parallel to $\boldsymbol{n}_0$, with one of them parallel to the platelet and one orthogonal to it. By numerically minimizing the elastic energy due to $\boldsymbol{n}(\boldsymbol{r})$ distortions (see Methods) that are created in response to the synchronous rotation of the thin platelet and the director at its surface within a large LC sample, we obtain the $\boldsymbol{n}(\boldsymbol{r})$ configuration shown in Fig. 1h and Extended Data Fig. 4. Multipole expansion analysis[15] for this $\boldsymbol{n}(\boldsymbol{r})$ yields only a strongly pronounced monopole moment, with higher-order multipole moments equal to zero up to numerical precision. The elastic charge of the monopole has the same sign as θ, and the strength of the monopole moment increases[8–10] with $|\theta|$ (see Methods).

Using laser tweezers and video microscopy, we probe the interactions of colloidal pairs (Fig. 2, Extended Data Fig. 5) by releasing particles with elastic charges of different strengths and signs from the laser traps near each other and at different orientations of the centre-to-centre separation vector $\boldsymbol{r}_c$ relative to $\boldsymbol{n}_0$. Unlike in electrostatics, like-charged elastic monopoles with the same signs of θ attract (Fig. 2a–c, Extended Data Fig. 5), but oppositely charged ones repel each other (Fig. 2d–f, Extended Data Fig. 5). This is consistent with the tendency of the LC

[1]Department of Physics, University of Colorado, Boulder, CO, USA. [2]Department of Electrical, Computer and Energy Engineering, University of Colorado, Boulder, CO, USA. [3]Soft Materials Research Center, University of Colorado, Boulder, CO, USA. [4]Renewable and Sustainable Energy Institute, National Renewable Energy Laboratory and University of Colorado, Boulder, CO, USA.
*e-mail: ivan.smalyukh@colorado.edu

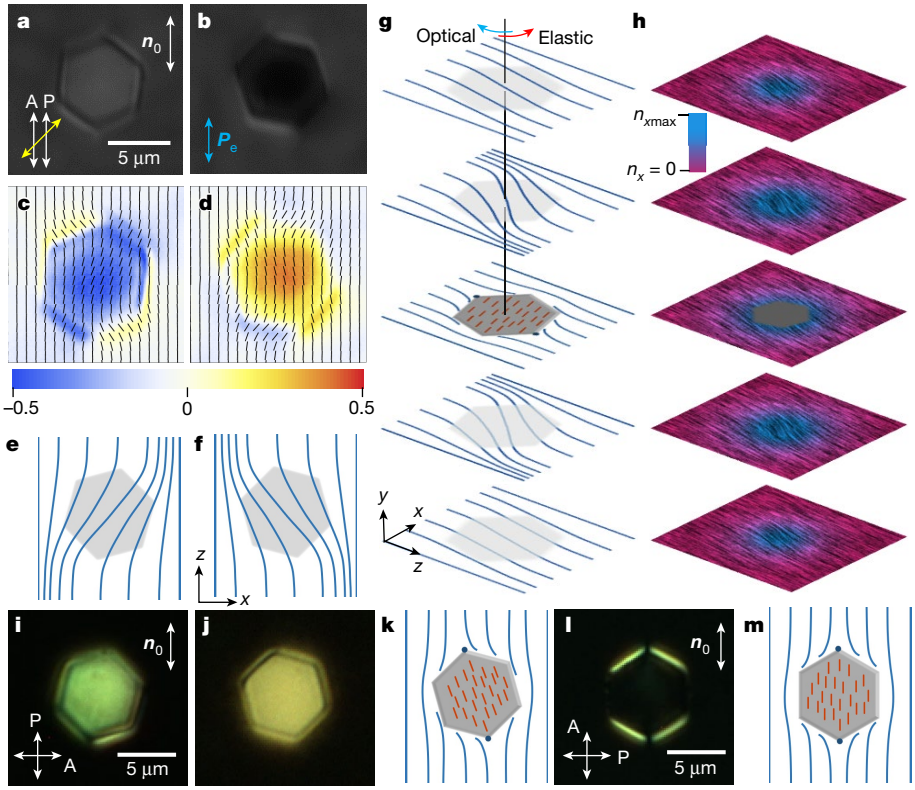

Fig. 1 | Oppositely charged elastic colloidal monopoles. a, **b**, Red-light polarizing optical micrographs of platelets with azobenzene surface monolayers in a nematic LC under an excitation light with its linear polarization $\boldsymbol{P}_e \| \boldsymbol{n}_0$. The labels 'P' and 'A' mark the linear polarization directions (white double arrows) of the polarizer and analyser of the microscope, respectively. The yellow double arrow shows the fast axis of a broadband quarter-wave plate. **c**, **d**, Patterns of the polarization state of red imaging light after it passes through the sample. Black rods indicate the long axes of the polarization ellipses. Colours represent ellipticity (see colour bar). **e**, **f**, Director field $\boldsymbol{n}(\boldsymbol{r})$ (blue lines) above the platelets for monopoles of opposite signs. **c** and **e** correspond to **a**; **d** and **f** correspond to **b**. **g**, Director field $\boldsymbol{n}(\boldsymbol{r})$ around the platelet; red rods show trans-state azobenzene molecules within the monolayers. Blue and red arrows indicate the optical and elastic torques, respectively. **h**, Numerically simulated pattern of the x component of $\boldsymbol{n}(\boldsymbol{r})$ corresponding to **g**. **i**, **j**, White-light polarizing micrographs at different platelet orientations for $\boldsymbol{P}_e \| \boldsymbol{n}_0$. **k**, Director field $\boldsymbol{n}(\boldsymbol{r})$ and azobenzene orientations corresponding to **j**. The director field for **i** is a mirror image of that shown in **k**. **l**, Micrograph of a platelet in the equilibrium state under white light with $\boldsymbol{P}_e \perp \boldsymbol{n}_0$. **m**, Director field $\boldsymbol{n}(\boldsymbol{r})$ and azobenzene orientations corresponding to **l**. Filled circles at the vertices of the platelets in **g**, **k** and **m** show surface point defects.

to minimize the distortions of $\boldsymbol{n}(\boldsymbol{r})$ when deviating away from $\boldsymbol{n}_0$ around the particles (Fig. 3a, b), where like-charged elastic monopoles with the same sense of particle rotation and sign of θ can reduce these elastic distortions when spatially co-located (Fig. 3b), whereas oppositely charged elastic monopoles can only minimize the free energy by increasing pair separation (Fig. 3a). Because our colloidal system is highly overdamped (Reynolds number much smaller than 1), the inertia effects are negligible and the elastic interaction forces are balanced by the viscous drag forces[11] ($f_d \propto dr_c/dt$). For a 2^l elastic multipole (here the integer l determines the order of the multipole), this balance with the elastic force $f_e \propto 1/r_c^{2l+2}$ results in the differential equation $dr_c/dt = -\alpha/r_c^{2l+2}$, which yields the anticipated time dependence of the inter-particle distance, $r_c(t) = [r_0^{2l+3} - (2l+3)\alpha t]^{1/(2l+3)}$, where r_0 is the initial centre-to-centre distance at the time of the release of the particles from the tweezers and α is a fitting parameter dependent on the particle's viscous drag and strength of multipole moments. For monopoles, $l = 0$ and $r_c(t) = (r_0^3 - 3\alpha t)^{1/3}$. Experimental data for $r_c(t)$, the interaction potential and the force versus the distance are consistent with the elastic monopole nature of the rotated particle (Fig. 2, Extended Data Fig. 5). As expected, elastic monopoles exhibit a pair potential proportional to $\pm 1/r_c$ (Fig. 2c, f, Extended Data Fig. 5). While the particles interact, the sign of their monopole moments can be switched by simply rotating the linear polarization of light in an opposite direction (Fig. 3a–c, Supplementary Video 1). Consequently, when this is done for one of the two interacting particles, the interactions are also switched from repulsion to attraction and vice versa (Fig. 3c). In addition, the Brownian motion of such a monopole platelet has a very different angular dependency of anisotropic diffusion relative to $\boldsymbol{n}_0$ compared with that of the platelet in the 'quadrupolar state' (Fig. 3d, e) because of the different symmetries of $\boldsymbol{n}(\boldsymbol{r})$ around monopolar and quadrupolar colloidal particles, as well as the particle orientation.

Remarkably, the intensity of the blue light needed to induce strong monopole moments and switch their signs is very low, with a power of less than 1 nW per particle (Fig. 3), as estimated by measuring the power of light uniformly illuminating the sample within the area of the platelet[25]. At slightly higher powers (>5 nW) of light shining on the particle pair[25], the interacting particles start a periodic rotational spinning while continuing to undergo elastic interactions mediated by the LC host medium (Fig. 4a–c, Supplementary Video 2). One can understand such periodic particle rotations as a result of an effective feedback mechanism that emerges from the rotation of the azobenzene moieties and the particle in response to polarized light. This particle rotation twists $\boldsymbol{n}(\boldsymbol{r})$ and consequently changes the polarization of light traversing the LC-embedded particle, which in turn further rotates the particle, and so on[25]. This out-of-equilibrium behaviour of a pair of colloidal objects leads to their dynamic self-assembly, where individual particles spin before approaching each other and after forming a colloidal dimer (Fig. 4a). This elastic interaction accompanied by spinning does not resemble the interaction of monopoles, but is consistent with the interaction of elastic quadrupoles (Fig. 4, Extended Data Fig. 6), with $r_c(t) = (r_0^7 - 7\alpha t)^{1/7}$ and an interaction potential proportional to $-1/r_c^5$. The spinning frequencies of the two particles are different, and their θ values (as well as the corresponding monopole moments) change between negative and positive values in an uncorrelated way

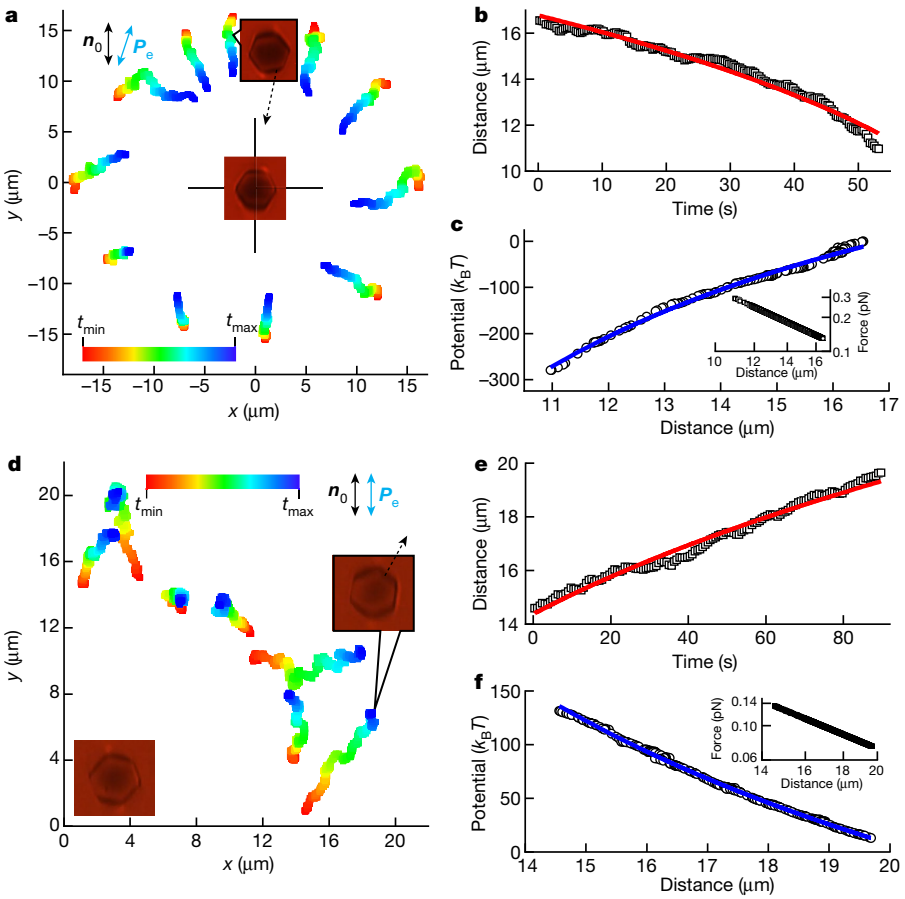

Fig. 2 | Colloidal interactions between elastic monopoles. a, Colour-coded trajectories of platelets after they are released from laser traps, showing attraction between monopoles of the same sign at all orientations of $\boldsymbol{r}_c$ relative to $\boldsymbol{n}_0$ within time periods of $t_{max} - t_{min} \approx 50$–$100$ s. The polarization of the excitation light $\boldsymbol{P}_e$ is at about 20° with respect to $\boldsymbol{n}_0$. The insets are micrographs of the interacting particles, and the black arrow indicates the direction of relative motion. **b**, Separation distance versus time for particles attracting along $\boldsymbol{n}_0$. **c**, Interaction potential versus distance corresponding to **b**; the inset shows a logarithmic plot of force versus distance. **d**, Omnidirectional repulsion between two monopoles of opposite signs, shown within one quadrant, for time periods of $t_{max} - t_{min} \approx 100$ s. **e**, Separation distance versus time for the trajectory indicated by the micrographs in **d**. **f**, Potential and force versus distance corresponding to **e**. Red curves in **b** and **e** are the best fits of the experimental data, with $r_c(t) = (r_0^3 - 3\alpha t)^{1/3}$ for $r_0 = 16.7$ μm, $\alpha = 19.7$ μm^3 s^{-1} (**b**) and $r_0 = 14.4$ μm, $\alpha = -15.8$ μm^3 s^{-1} (**e**). Blue curves in **c** and **f** are the best fits to a potential function proportional to $1/r_c$. The elastic charges estimated from the fits are 0.49 μm (**b**) and 0.44 μm (**e**). The micrographs in the insets of **a** and **d** are scaled so that their dimensions match the coordinate axes.

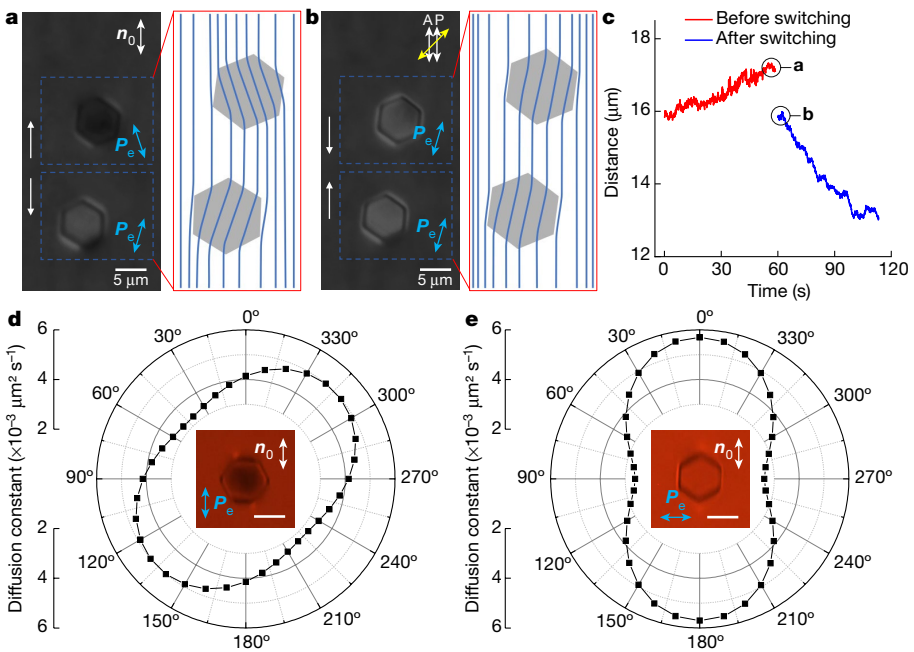

Fig. 3 | Optical switching of the signs and strengths of interactions of the elastic monopoles. a, Micrograph (left) and corresponding schematic (right) of $\boldsymbol{n}(\boldsymbol{r})$, showing elastic monopoles of opposite signs, induced by exposure to linearly polarized blue light at different polarizations. Regions exposed to differently polarized blue light are shown in dashed boxes, with the linear polarization directions marked by blue double arrows. The pair of white arrows on the left shows the interaction forces. **b**, Micrograph (left) and corresponding schematic (right) of $\boldsymbol{n}(\boldsymbol{r})$, showing elastic monopoles of the same sign, switched from their initial state (shown in **a**) by changing the polarization of blue light to be the same for both platelets. The sign of the monopole of the upper particle is then flipped, and so is the direction of the interaction force. **c**, Separation distance versus time before and after switching (at 58 s after the release of the platelets from the laser traps). Points circled and marked '**a**' and '**b**' correspond to the micrographs shown in **a** and **b**. **d**, **e**, Angular dependence of the diffusion constant of a platelet at $\boldsymbol{P}_e \| \boldsymbol{n}_0$ (**d**) and $\boldsymbol{P}_e \perp \boldsymbol{n}_0$ (**e**); scale bars in the insets are 5 μm.

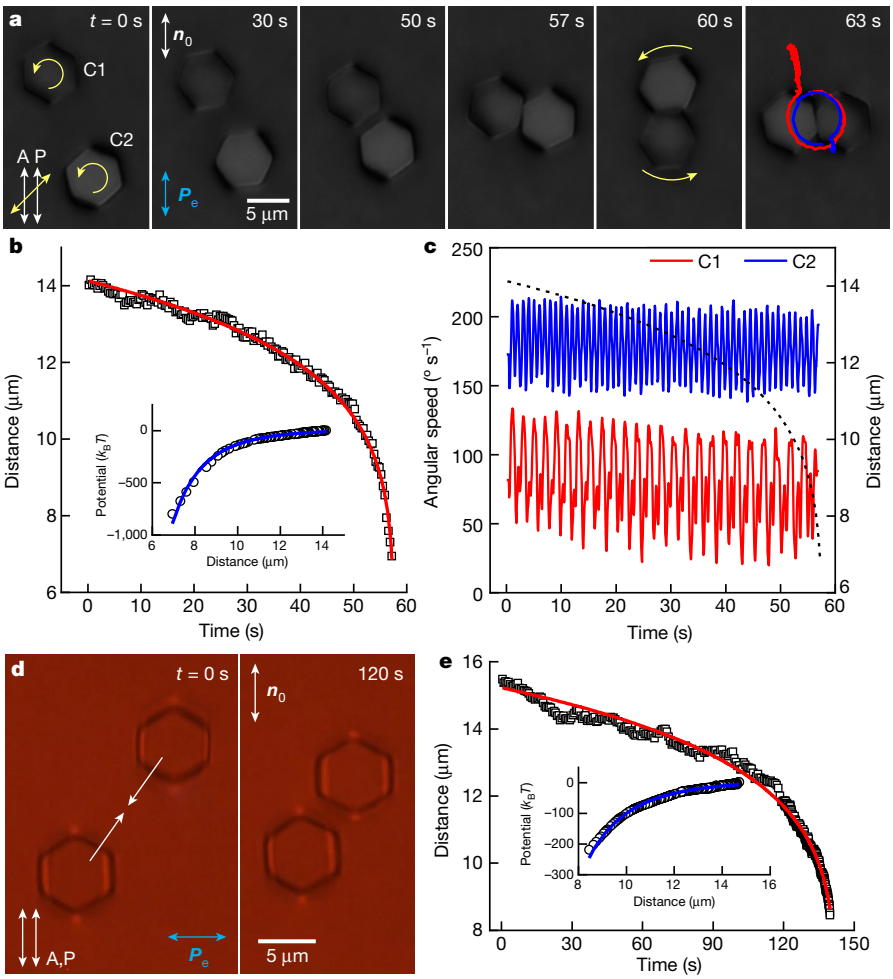

Fig. 4 | Out-of-equilibrium colloidal assembly. a, Time-stamped micrographs showing two colloidal platelets (C1 and C2) attracting and assembling while spinning with $\boldsymbol{P}_e \| \boldsymbol{n}_0$. Red and blue lines in the last micrograph show the trajectories of the two particles (red for C1 and blue for C2). **b**, Separation distance versus time of attracting particles until the moment of contact for the platelets shown in **a**. The inset shows the interaction potential versus the distance. **c**, Angular speed of the two spinning particles shown in **a**, both exhibiting periodic motion but at different frequencies. The black dashed line indicates the distance between C1 and C2 versus time, extracted from **b**. **d**, Micrographs of platelets attracting diagonally with respect to $\boldsymbol{n}_0$ at $\boldsymbol{P}_e \perp \boldsymbol{n}_0$ at different positions. **e**, Separation distance versus time corresponding to **d**; the inset shows the interaction potential versus the distance. Red curves in **b** and **e** are the best fits of the experimental data with $r_c(t) = (r_0^7 - 7\alpha t)^{1/7}$ for $r_0 = 14.1\ \mu m$, $\alpha = 2.79 \times 10^5\ \mu m^7\ s^{-1}$ (**b**) and $r_0 = 15.2\ \mu m$, $\alpha = 1.91 \times 10^5\ \mu m^7\ s^{-1}$ (**e**). Blue curves in **b** and **e** are the best fits with the potential proportional to $-1/r_c^5$.

and on timescales much shorter than the time of the long-range interaction (Fig. 4b, c). Therefore, the instantaneous elastic monopole moments periodically switch from like-charged to oppositely charged and, on average, do not contribute to the observed behaviour (Fig. 4b). The ensuing scaling of the pair interaction potential as $-1/r_c^5$ is similar to that obtained for a linear polarization of the excitation/imaging light, $\boldsymbol{P}_e$, orthogonal to $\boldsymbol{n}_0$ (Fig. 4d, e, Extended Data Fig. 6) or when only red—but not violet or blue—light is used, which corresponds to quadrupolar nematic colloids (Fig. 1l, m).

Light with a linear polarization of $\boldsymbol{P}_e \| \boldsymbol{n}_0$ traverses the LC as an extraordinary eigenmode (Fig. 1a, b). As it reaches the platelet with the azobenzene molecular monolayers, it torques the trans-state moieties of the dye molecules to rotate and align them orthogonally[25,27] to $\boldsymbol{P}_e \| \boldsymbol{n}_0$, driven by the tendency of azobenzene to avoid the excited state[28]. Owing to the mechanical coupling between the azobenzene monolayer and $\boldsymbol{n}(\boldsymbol{r})$ through surface anchoring, a platelet is prompted to rotate, albeit this rotation further increases $\boldsymbol{n}(\boldsymbol{r})$ distortions around the platelet (Fig. 1). The optical torque, transferred to the platelet through surface anchoring, is then balanced by the elastic torque, which tends to minimize the free energy of elastic distortions (Fig. 1g, Extended Data Fig. 1). In addition to numerical modelling (Fig. 1h, Extended Data Fig. 4), approximating the platelet by a high-aspect-ratio disk of radius R, the strength of the elastic torque due to the local rotation of the director by the platelet to an angle θ can be estimated using the theory of Brochard and de Gennes[24] as $T_e = 8KR\theta$, where K is the average elastic constant of the LC. Consistent with our numerical modelling (Extended Data Fig. 7) and experiments (Fig. 1c,d), the rotated platelet is accompanied by a twisted $\boldsymbol{n}(\boldsymbol{r})$ around it, whereas adiabatic rotation of the nearly linear polarization of the light closely follows this twisted $\boldsymbol{n}(\boldsymbol{r})$ above and below the platelet, albeit slightly lagging it[29]. Under these conditions, for independently measured material and geometric parameters (see Methods), the competition of optical and elastic torques yields a torque-balancing angle of $\theta_{tb} \approx 26°$, which agrees with experiments (Fig. 1), as well as the excited-state elastic monopoles.

Although our monopoles and samples are three-dimensional in nature, to facilitate direct optical microscopy observations of their colloidal behaviour, the geometry of our experiments is designed as quasi-two-dimensional, because elastic monopoles and quadrupoles are repelled from confining cell substrates with strong surface boundary conditions[20] for a director along $\boldsymbol{n}_0$. These boundary conditions and confinement also tend to align the large-area faces of the platelets to be parallel to the confining substrates, facilitating their self-assembly within the mid-plane of the sample. The direction of light illumination is orthogonal to both the platelets and the confining substrates, defining

the axis of platelet rotation that distorts $\boldsymbol{n}(\boldsymbol{r})$. Without the influence of the confining plates, the interactions between platelets and other anisotropic colloidal objects should depend on their relative orientations, in a manner that has more structure than a simple scalar elastic charge. It will be of interest to extend and generalize our study to LC colloids without such confinement (which also causes screening of elastic interactions at large inter-particle distances) and with different geometric shapes, because the combination of LCs and particle anisotropy may lead to a richer behaviour than that observed in the electrostatic analogues of our colloids.

To conclude, we have designed, demonstrated and explained elastic colloidal monopoles in LCs, which can be induced by ambient light and have switchable sign and amplitude of the monopole moment. We have shown how like-charged elastic monopoles attract and oppositely charged ones repel, how these interactions can be switched from attractive to repulsive and how monopoles can be transformed to quadrupoles by invoking the highly reconfigurable nature of our LC colloids. Our work is a contribution towards the development of soft-matter analogues of Rydberg matter[16], where colloidal particles can self-assemble while in out-of-equilibrium states into structures different from those that they would form under equilibrium conditions, although very different in terms of length and energy scales from those in atomic Rydberg matter. This may enable out-of-equilibrium excited-state self-assembly of composite materials based on LCs and may lead to new types of active matter[30].

Online content

Any methods, additional references, Nature Research reporting summaries, source data, statements of data availability and associated accession codes are available at https://doi.org/10.1038/s41586-019-1247-7.

Received: 3 January 2019; Accepted: 5 April 2019;
Published online 29 May 2019.

1. Milo, R. & Phillips, R. *Cell Biology by the Numbers* (Garland Science, 2015).
2. Poon, W. Colloids as big atoms. *Science* **304**, 830–831 (2004).
3. Frenkel, D. Playing tricks with designer atoms. *Science* **296**, 65–66 (2002).
4. Chaikin, P. M. & Lubensky, T. C. *Principles of Condensed Matter Physics* (Cambridge Univ. Press, 1995).
5. de Gennes, P. G. & Prost, J. *The Physics of Liquid Crystals* 2nd edn (Clarendon Press, 1993).
6. Poulin, P., Stark, H., Lubensky, T. C. & Weitz, D. A. Novel colloidal interactions in anisotropic fluids. *Science* **275**, 1770–1773 (1997).
7. Smalyukh, I. I. Liquid crystal colloids. *Annu. Rev. Condens. Matter Phys.* **9**, 207–226 (2018).
8. Lubensky, T. C., Pettey, D., Currier, N. & Stark, H. Topological defects and interactions in nematic emulsions. *Phys. Rev. E* **57**, 610–625 (1998).
9. Lev, B. I. & Tomchuk, P. M. Interaction of foreign macrodroplets in a nematic liquid crystal and induced supermolecular structures. *Phys. Rev. E* **59**, 591–602 (1999).
10. Pergamenshchik, V. M. & Uzunova, V. A. Colloidal nematostatics. *Condens. Matter Phys.* **13**, 33602 (2010).
11. Loudet, J. C., Hanusse, P. & Poulin, P. Stokes drag on a sphere in a nematic liquid crystal. *Science* **306**, 1525 (2004).
12. Ruhwandl, R. W. & Terentjev, E. M. Long-range forces and aggregation of colloid particles in a nematic liquid crystal. *Phys. Rev. E* **55**, 2958 (1997).
13. Senyuk, B., Puls, O., Tovkach, O., Chernyshuk, S. & Smalyukh, I. I. Hexadecapolar nematic colloids. *Nat. Commun.* **7**, 10659 (2016).
14. Jackson, J. D. *Classical Electrodynamics* 3rd edn (Wiley, 1998).
15. Senyuk, B., Aplinc, J., Ravnik, M. & Smalyukh, I. I. High-order elastic multipoles as colloidal atoms. *Nat. Commun.* **10**, 1825 (2019).
16. Sakurai, J. J. & Tuan, S. F. *Modern Quantum Mechanics* (Addison-Wesley, 1994).
17. Loudet, J. C. & Poulin, P. Application of an electric field to colloidal particles suspended in a liquid-crystal solvent. *Phys. Rev. Lett.* **87**, 165503 (2001).
18. Stark, H. Director field configurations around a spherical particle in a nematic liquid crystal. *Eur. Phys. J. B* **10**, 311–321 (1999).
19. Zhou, Y., Senyuk, B., Zhang, R., Smalyukh, I. I. & de Pablo, J. J. Degenerate conic anchoring and colloidal elastic dipole-hexadecapole transformations. *Nat. Commun.* **10**, 1000 (2019).
20. Senyuk, B., Liu, Q., Nystrom, P. D. & Smalyukh, I. I. Repulsion–attraction switching of nematic colloids formed by liquid crystal dispersions of polygonal prisms. *Soft Matter* **13**, 7398–7405 (2017).
21. Lee, B., Kim, S., Kim, J. & Lev, B. Coulomb-like elastic interaction induced by symmetry breaking in nematic liquid crystal colloids. *Sci. Rep.* **7**, 15916 (2017).
22. Nikkhou, M. et al. Light-controlled topological charges in a nematic liquid crystal. *Nat. Phys.* **11**, 183–187 (2015).
23. Nikkhou, M., Škarabot, M. & Muševič, I. Annihilation dynamics of topological monopoles on a fiber in nematic liquid crystals. *Phys. Rev. E* **93**, 062703 (2016).
24. Brochard, F. & de Gennes, D. G. Theory of magnetic suspensions in liquid crystals. *J. Phys.* **31**, 691–708 (1970).
25. Yuan, Y., Abuhaimed, G. N., Liu, Q. & Smalyukh, I. I. Self-assembled nematic colloidal motors powered by light. *Nat. Commun.* **9**, 5040 (2018).
26. Dong, M., Babalhavaeji, A., Samanta, S., Beharry, A. A. & Woolley, G. A. Red-shifting azobenzene photoswitches for in vivo use. *Acc. Chem. Res.* **48**, 2662–2670 (2015).
27. Yi, Y., Farrow, M., Korblova, E., Walba, D. M. & Furtak, T. E. High-sensitivity aminoazaobenzene chemisorbed monolayers for photoalignment of liquid crystals. *Langmuir* **25**, 997–1003 (2009).
28. Natansohn, A. & Rochon, P. Photoinduced motions in azo-containing polymers. *Chem. Rev.* **102**, 4139–4176 (2002).
29. Yeh, P. & Gu, C. *Optics of Liquid Crystal Displays* (John Wiley & Sons, 1999).
30. Ramaswamy, S. The mechanics and statistics of active matter. *Annu. Rev. Condens. Matter Phys.* **1**, 323–345 (2010).

Acknowledgements We thank P. Ackerman, A. Hess, S. Park, J.-S. Tai and M. Tasinkevych for technical assistance and discussions. This research was supported by the US Department of Energy, Office of Basic Energy Sciences, Division of Materials Sciences and Engineering, under Award ER46921, contract DE-SC0019293 with the University of Colorado at Boulder.

Reviewer information *Nature* thanks Dong Ki Yoon and the other anonymous reviewer(s) for their contribution to the peer review of this work.

Author contributions Y.Y. and Q.L. synthesized the azobenzene-containing dye molecules. Q.L. fabricated the colloidal particles. Y.Y. and B.S. performed the experiments and Y.Y. performed the numerical modelling. Y.Y., B.S. and I.I.S. analysed the data. I.I.S. conceived the idea and directed the project, designed the experiments, provided funding and wrote the manuscript, with the input from all authors.

Competing interests The authors declare no competing interests.

Additional information
Extended data is available for this paper at https://doi.org/10.1038/s41586-019-1247-7.
Supplementary information is available for this paper at https://doi.org/10.1038/s41586-019-1247-7.
Reprints and permissions information is available at http://www.nature.com/reprints.
Correspondence and requests for materials should be addressed to I.I.S.
Publisher's note: Springer Nature remains neutral with regard to jurisdictional claims in published maps and institutional affiliations.

METHODS

Sample preparation. The photo-responsive azobenzene molecules were synthesized by combining 2.70 g of methyl red, 2.22 g of 1,3-dicyclohexylcarbodiimide and 2.38 mL of (3-aminopropyl) triethoxysilane in 60 mL of dichloromethane under nitrogen[27]. The resulting solution was stirred overnight and filtered, after which column chromatography (50% ethyl acetate and 50% hexane in volume) and rotary evaporation were used to isolate and purify the obtained azobenzene-containing dye molecules. To fabricate hexagonal silica micro-platelets, a 0.5-μm-thick silica layer was first deposited on a silicon wafer by plasma-enhanced chemical vapour deposition and then an additional layer of photoresist AZ5214 was obtained by spin-coating. Particle shapes were then defined on the photoresist layer by a direct laser writing system (DWL 66FS, Heidelberg Instruments). Finally, free-standing silica platelets were carved out of the substrate by inductively coupled plasma etching after removal of the photoresist by acetone. The photosensitive azobenzene molecular monolayers were self-assembled on hydroxylated surfaces of the platelets. To achieve this, the micro-platelets, while still on the substrate, were first treated in piranha solution (98 wt% sulfuric acid and 30 wt% hydrogen peroxide, volume ratio 1:1) for 1 h, rinsed thoroughly with deionized water and dried at 70 °C for 1 h. Subsequently, the platelets were immersed in 20 mL of a 0.53 mM toluene solution of the azobenzene molecules, followed by injecting 20 μL of *n*-butylamine. After reacting overnight at 45 °C, the platelets were rinsed with toluene and cured at 120 °C for 2 h. An isopropanol suspension of the functionalized platelets was obtained by ultrasonication to release them from the substrate and was then mixed with a nematic LC. The mixture was left at room temperature uncovered to allow the solvent to evaporate, eventually yielding the LC colloidal dispersion. The resulting dispersion was then sandwiched between glass plates separated by glass spacers with a diameter of 4–16 μm and sealed with epoxy. Prior to this, thin layers of polyimide (PI2555, from HD Microsystem) were spin-coated on the glass plates and rubbed unidirectionally to define the planar boundary conditions and orient the far-field director $\boldsymbol{n}_0$ along the rubbing direction. All chemicals used were obtained from Sigma-Aldrich unless noted otherwise.

Experimental imaging, laser trapping and illumination setup. Polarizing optical microscopy and video microscopy of the colloidal interactions between the platelets were performed using a home-made micro-projection system built using an upright microscope (BX51, Olympus) and LC microdisplays extracted from a consumer colour projector (EMP-730, Epson) (Extended Data Fig. 2). Because observation with a conventional white-light microscope prompts the rotation of platelets and induces monopoles, we additionally studied our nematic colloids with illumination from a narrow-band optical microscope specially designed to preclude its interaction with the azobenzene monolayers and particles. Owing to azobenzene's sensitivity to violet-blue light (Extended Data Fig. 3a), red light—provided by filtering the microscope illumination with a bandpass filter (FF01-640/14-25, Semrock)—was used for imaging and observation in this case. After passing through the sample, the imaging light was collected by high-numerical-aperture objective lenses with a magnification of 20× to 60× (Olympus) and directed to a charge-coupled device (CCD) camera (Grasshopper3, PointGrey) to record images and videos. The blue excitation light that controllably rotated the azobenzene molecules and twisted the director field was produced by projecting patterns designed in Microsoft PowerPoint slides and projected using the LC microdisplays[31] (Extended Data Fig. 2). The polarization of the projected blue light was controlled by rotatable linear polarizers inserted within the optical path of the two illumination channels. The generation and switching of elastic monopoles with opposite signs requires the ability to locally control the polarization state of blue light projected within the field of view of a microscope, at scales comparable to the particle dimensions. In our experiments, this was achieved using the home-built setup shown in Extended Data Fig. 2. The mutually orthogonal linear polarizations of the blue light from the two separately controlled channels of the setup were separated using a polarizing beam-splitter cube (CCM1-PB251, obtained from Thorlabs) after exiting the projector. Additional retardation plates and linear polarizers inserted into the two light paths enabled independent control of the polarization within two patterns separately generated by two microdisplays. Light rays from the two channels were then recombined with a 50/50 plate beam splitter (BSW10R, from Thorlabs) before entering the microscope and projected to the sample, which was placed on a microscope stage within the same field of view of an objective. Using this setup, we illuminated sample areas with blue-light patterns with controlled linear polarization states. This allowed us to illuminate particles in proximity of each other using blue light with linear polarization states controlled independently. Integrated with the illumination and imaging setup, laser tweezers operating at 1,064 nm and 1–100 mW (YLR-10-1064, IPG Photonics) allowed us to set the appropriate initial conditions for the platelets suspended in LC to probe colloidal pair interactions. The trajectories of individual particles in the videos taken under a microscope were extracted using the freeware ImageJ (obtained from the National Institute of Health). Details of the setup and operation of the laser tweezers are provided in ref. [20].

Characterization of colloidal diffusion and pair interactions. The intrinsic anisotropy of the LC host, the anisotropic shape of the studied particles, and the formation of defects and director distortions all contribute to the anisotropic Brownian motion of the colloidal platelets (Fig. 3d, e). Interestingly, this anisotropic Brownian motion can be further altered by tuning the polarization of the blue excitation light, as characterized by the angular dependence of the diffusion constant (Fig. 3d, e). The diffusion constants D were calculated on the basis of single-particle Brownian motion statistics by fitting the displacement histogram with a Gaussian function[20,32], yielding the Stokes drag coefficients at different directions relative to $\boldsymbol{n}_0$ according to $c = k_BT/D$, where $T = 300$ K is the temperature and $k_B = 1.38 \times 10^{-23}$ J K^{-1} is the Boltzmann constant. For simplicity, an average value of $c = 10^{-6}$ kg s^{-1} was often used in the analysis of forces and potentials. The viscous drag force was calculated using the speed of the colloidal platelet, $v = \mathrm{d}r_c/\mathrm{d}t$, according to $f_d = cv$ and was balanced by the elastic force between the interacting particles (because of the highly overdamped motion, as discussed in the main text). This allowed us to determine the distance dependence of the potential and force of the elastic colloidal interaction, which were both found to be in agreement with theoretical expectations based on the electrostatic analogy (Figs. 2, 4, Extended Data Fig. 5).

The monopole-type nature of the particles was revealed and the strength of the elastic charges was estimated by fitting the experimental data with the power-law functions of the monopole–monopole interaction. Similarly to electrostatics[14], the force between two elastic charges of strength Q is[9,10]

$$f_e = \pm 4\pi K \frac{Q^2}{r_c^2} \tag{1}$$

where K is the average elastic constant of the LC and the sign depends on the relative sign of the elastic charges. One can define a parameter

$$\alpha = \pm 4\pi K Q^2/c \tag{2}$$

so that the force balance equation $f_d + f_e = 0$ is reduced to

$$\frac{\mathrm{d}r_c}{\mathrm{d}t} = -\frac{\alpha}{r_c^2} \tag{3}$$

which is integrated to give the equation of motion

$$r_c(t) = (r_0^3 - 3\alpha t)^{1/3} \tag{4}$$

where r_0 is the initial separation upon releasing the interacting particles from the laser traps. Using the average elastic constant of 4'-*n*-pentyl-4-cyanobiphenyl (5CB), $K = 6.5$ pN, and a value of α obtained from fitting experimental data of separation distance versus time, one obtains the magnitude of the corresponding elastic charge

$$Q = \sqrt{\frac{|\alpha|\, c}{4\pi K}} \tag{5}$$

which was found to be about 0.5 μm in our experiments (Fig. 2, Extended Data Fig. 5).

On the other hand, elastic charges—or, in general, the strength of multipole moments—can be calculated directly using the known far-field director configurations. To do this, we considered a spherical surface enclosing the platelet with radius $a \gg R$, where R is the effective lateral size of the platelet, so that director deviation away from $\boldsymbol{n}_0 = (0, 0, 1)$ is small. Assuming that the director orientation on this surface is uniform, $\boldsymbol{n}_S = (\sin\theta_S, 0, \cos\theta_S)$, the total charge is given by[10]

$$Q = \frac{a}{4\pi}\int \mathrm{d}S \frac{\sin\theta_S}{a^2} = a\sin\theta_S \approx a\theta_S \tag{6}$$

where θ_S is small and $\cos\theta_S \approx 1$. At a distance of $a = 10$ μm, the director orientation angle is $\theta_S = 3°$, which is closely related to how strongly the platelet perturbs $\boldsymbol{n}(\boldsymbol{r})$, that is, the platelet rotation angle θ.

Polarimetric imaging and analysis. The birefringence of LCs and the distortion of the director due to colloidal inclusions cause changes in the polarization state of the light traversing the sample[29,33]. These changes are monitored by polarimetric imaging of the exiting light in the experiments when using linearly polarized incoming light. To perform polarimetric imaging, a quarter-wave plate (AQWP05M-600, obtained from Thorlabs) was inserted immediately below the microscope's analyser, whose polarization was set along the far-field director $\boldsymbol{n}_0$. Images were taken when the fast axis of the quarter-wave plate was rotated from 0° (defined with respect to $\boldsymbol{n}_0$) to 180° at steps of 22.5°. These images were processed numerically to calculate the ellipticity and orientation of the polarization ellipses of the outgoing light[33]. The image analysis process is summarized as follows. Assuming the angle at which the fast axis of the quarter-wave plate was rotated to be β_n ($\beta_n = 22.5°n$, $n = 1, \ldots, N = 8$), four coefficients were defined for each pixel of images

$$C_1 = \frac{2}{N}\sum_{n=1}^{8} I_n \tag{7}$$

$$C_2 = \frac{4}{N}\sum_{n=1}^{8} I_n \sin(2\beta_n) \tag{8}$$

$$C_3 = \frac{4}{N}\sum_{n=1}^{8} I_n \cos(4\beta_n) \tag{9}$$

$$C_4 = \frac{4}{N}\sum_{n=1}^{8} I_n \sin(4\beta_n) \tag{10}$$

from which the Stokes parameters[29] were calculated on a pixel-by-pixel basis as follows

$$S_0 = C_1 - C_3,\ S_1 = 2C_3,\ S_2 = 2C_4,\ S_3 = C_2 \tag{11}$$

Images captured by the CCD camera at different angles β_n provided the values for the intensity, I_n, and thus enabled the reconstruction of the polarization states of the exiting imaging light after passing through the sample on a pixel-by-pixel basis (Fig. 1c, d). For this, the ellipticity e and the orientation angle χ of the polarization ellipse (defined as the angle between the long axis of the polarization ellipse and $\boldsymbol{n}_0$) were obtained using $\sin(2e) = S_3/S_0$ and $\tan(2\chi) = S_2/S_1$ on a pixel-by-pixel basis (Fig. 1c, d). Two-dimensional polarimetric images like the ones shown in Fig. 1c, d were formed by overlaying the plots of the orientation patterns of the long axis of the ellipse (black rods) and the ellipticity (colour bar).

Estimation of the platelet's torque-balancing rotation angle. Disregarding the energetic costs of director distortions near the edge faces of our thin platelets, the elastic energy due to the twist of the director around the rotated platelets can be estimated using the model developed by Brochard and de Gennes for small inclusions in LCs that exert a torque on the director structure[24], which gives

$$F_e = 2\pi KC\theta^2 \tag{12}$$

where C is the effective 'capacitance' of the particle (we note that this expression was also derived using electrostatic analogies) and θ is the net maximum twist angle of the director with respect to $\boldsymbol{n}_0$, which is also assumed to be the angle to which a platelet rotates upon exposure to the blue light. The capacitance of the thin hexagonal platelets used in this study can be approximated to be that of high-aspect-ratio disks[34], $C = 2R/\pi$. Therefore, the elastic torque from the director distortion caused by balancing of the optical torque is

$$T_e = \frac{\partial F_e}{\partial \theta} = 8KR\theta \tag{13}$$

The free-energy potential describing the coupling between polarized blue light and director orientation through the azobenzene monolayers can be expressed as[25]

$$F_p = \frac{1}{2}\sigma(I,e)\int \mathrm{d}S\,(\boldsymbol{P}_p \cdot \boldsymbol{n}_p)^2 \tag{14}$$

where $\sigma(I, e)$ characterizes the anchoring strength of the surface of the monolayers, and depends on the intensity I and ellipticity e of the blue light reaching the surface of the platelet[25]. In the expression above, $\boldsymbol{P}_p$ is the orientation of the long axis of the polarization ellipse of the blue light and $\boldsymbol{n}_p$ is the orientation of $\boldsymbol{n}(\boldsymbol{r})$ at the surface of the platelet. Assuming uniform $\boldsymbol{n}_p$ across the large-area surface of the platelet, the free-energy potential is simplified to

$$F_p = \frac{1}{2}\sigma(I,e)\int \mathrm{d}S\cos^2\phi = \frac{1}{2}\sigma(I,e)\,2A\cos^2\phi \tag{15}$$

where ϕ is the angle between $\boldsymbol{P}_p$ and $\boldsymbol{n}_p$ and A is the area of the hexagonal surface of the platelet. The factor of 2 accounts for the presence of 2 (top and bottom) photoresponsive surfaces interfacing the LC surfaces. Following the procedures described in ref. [29], the angle ϕ characterizing the close-to-linear polarization state of light traversing the platelet is calculated using the Jones matrix method

$$\phi = \frac{1}{2}\tan^{-1}\frac{2\theta X \tan X}{(\theta^2 - \Gamma^2/4)\tan^2 X - X^2} \tag{16}$$

where

$$\Gamma = \frac{2\pi\Delta n d}{\lambda},\ X = \sqrt{\theta^2 + \left(\frac{\Gamma}{2}\right)^2} \tag{17}$$

and where $d = 12\,\mu$m is the LC thickness through which the blue light propagates before reaching the top surface of the platelet, $\lambda = 490$ nm is the wavelength of the blue light and $\Delta n = 0.2$ is the birefringence of 5CB. The value of Γ is found to be 30.8, much larger than that of θ, with both expressed in radians (experimental observation indicates that θ is usually in the range of 30°, or about 0.52 rad, or less, as shown in Fig. 1). In this case, ϕ is approximated by taking the first two non-zero terms of the Taylor expansion for $\lim_{\theta/\Gamma\to 0}\phi = 0$

$$\phi \approx -\frac{1}{2}\left[0.91\frac{2\theta}{\Gamma} + 0.42\left(\frac{2\theta}{\Gamma}\right)^3\right] \tag{18}$$

The corresponding optical torque transferred to the platelets through anisotropic surface interactions and causing platelet rotation is

$$T_p = \frac{\partial F_p}{\partial \phi}\bigg|_{\phi\approx 0} \approx -2\sigma A\phi \tag{19}$$

Balancing the optical torque and the elastic torque under the equilibrium conditions allows us to find the platelet rotation angle analytically by assuming $A = \pi R^2$

$$\theta_{tb} = \frac{\Gamma}{2}\sqrt{\left(\frac{4K\Gamma}{\pi\sigma R} - 0.91\right)/0.42} \tag{20}$$

Using the average elastic constant of 5CB, $K = 6.5$ pN, $R = 2.8\,\mu$m and $\sigma = 10^{-4}$ J m^{-2}, we obtain the experiment-matching torque-balancing angle $\theta_{tb} = 26°$, where the surface anchoring strength σ at a light intensity of 1 nW was estimated independently.

Numerical modelling of director configurations and polarization states. Computer simulations of the director distortion induced by the azobenzene-capped platelets were based on the minimization of the Frank–Oseen free energy[5]

$$F = \int dV\left(\frac{1}{2}K_{11}(\nabla\cdot\boldsymbol{n})^2 + \frac{1}{2}K_{22}(\boldsymbol{n}\cdot\nabla\times\boldsymbol{n})^2 + \frac{1}{2}K_{33}(\boldsymbol{n}\times\nabla\times\boldsymbol{n})^2 - K_{24}\{\nabla\cdot[\boldsymbol{n}(\nabla\cdot\boldsymbol{n}) + \boldsymbol{n}\times(\nabla\times\boldsymbol{n})]\}\right) \tag{21}$$

where the Frank elastic constants K_{11}, K_{22}, K_{33} and K_{24} describe the energetic costs of the splay, twist, bend and saddle-splay deformations of the director field $\boldsymbol{n}(\boldsymbol{r})$. This modelling was done under the assumption of infinitely thin platelets with fixed, uniform in-plane boundary conditions, with the platelets rotated to θ_{tb} with respect to their orientation under no-illumination light conditions. Following ref. [35], a large grid size of $101 \times 101 \times 101$ was used with grid spacing of $h_x = h_y = h_z = 0.5\,\mu$m. The far-field director was set to $\boldsymbol{n}_0 = (0, 0, 1)$ with fixed boundary conditions at the top and bottom (x–z plane) and periodic boundary conditions in the lateral directions (x–y and y–z planes) of the computational box. At the central grid point with coordinates (51, 51, 51), the orientation of the director was fixed at an angle of $\theta_n = 30°$ or 45° with respect to $\boldsymbol{n}_0$, that is, $\boldsymbol{n} = (\sin\theta_n, 0, \cos\theta_n)$, while the director at the surrounding grid points was allowed to re-orient accordingly during the simulation. Relaxation of this initial condition yielded a director perturbation that decayed as $1/r$ (Extended Data Fig. 4) and the monopole moment being the only non-zero multipole moment up to the computational precision.

The propagation of light through such distorted director structures was modelled using the Jones matrix method[29]. To better model the real experimental system, where gravity shifts the platelet downwards with respect to the mid-plane of the LC cell, the director region with a strong twist was placed closer to the bottom of the computational box, with the director field across the sample thickness parameterized as $\boldsymbol{n} = (\sin\theta_n, 0, \cos\theta_n)$. After obtaining the director structure using the approach described above, the Jones matrix method was applied assuming that each grid point represented a thin layer of 0.16-μm-thick LC with a uniform optical axis defined by the local director orientation $\boldsymbol{n}(\boldsymbol{r})$. This grid spacing of 0.16 μm resulted in a total cell thickness of 16 μm, as used in the experiments, and an initial twist of about 3 μm above the bottom substrate. Then the polarization states of the red imaging light ($\lambda = 640$ nm) were calculated on a point-by-point basis by propagating the light sequentially through the layers in the y direction. Given an incident polarization of $\boldsymbol{P}_i \| \boldsymbol{n}_0$, the distribution of the ellipticity e and the orientation angle χ of the polarization ellipses were obtained, which correspond to the change of the polarization states as the director perturbation decays away from the edge of the particle (Extended Data Fig. 7). These results are consistent with our polarimetric measurements (Fig. 1c, d).

Data availability

All data generated or analysed during this study are included in the published article and its Supplementary Information and are available from the corresponding author upon reasonable request.

Code availability

The codes used in this study for the numerical simulation and calculation are available upon request.

31. Martinez, A., Mireles, H. C. & Smalyukh, I. I. Large-area optoelastic manipulation of colloidal particles in liquid crystals using photoresponsive molecular surface monolayers. *Proc. Natl Acad. Sci. USA* **108**, 20891–20896 (2011).
32. Senyuk, B., Glugla, D. & Smalyukh, I. I. Rotational and translational diffusion of anisotropic gold nanoparticles in liquid crystals controlled by varying surface anchoring. *Phys. Rev. E* **88**, 062507 (2013).
33. Schaefer, B., Collett, E., Smyth, R., Barrett, D. & Fraher, B. Measuring the Stokes polarization parameters. *Am. J. Phys.* **75**, 163–168 (2007).
34. Rovner, J. B., Borgnia, D. S., Reich, D. H. & Leheny, R. L. Elastic and hydrodynamic torques on a colloidal disk within a nematic liquid crystal. *Phys. Rev. E* **86**, 041702 (2012).
35. Ackerman, P. J. & Smalyukh, I. I. Diversity of knot solitons in liquid crystals manifested by linking of preimages in torons and hopfions. *Phys. Rev. X* **7**, 011006 (2017).

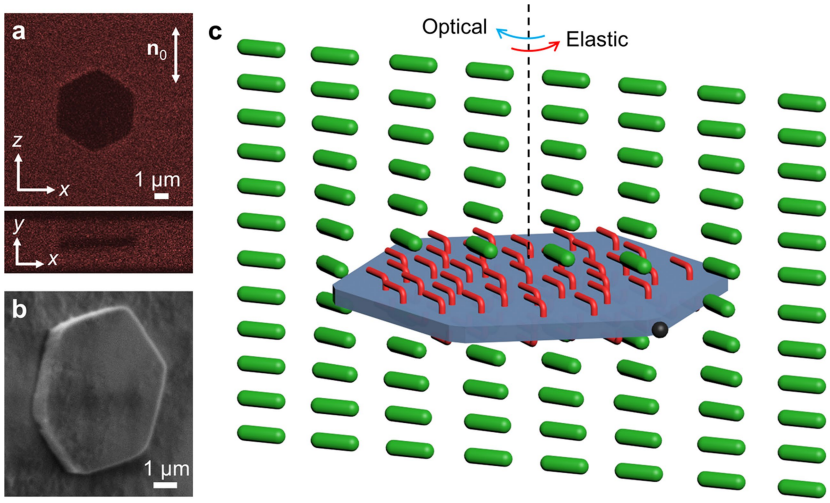

Extended Data Fig. 1 | Hexagonal colloidal platelet with azobenzene monolayers dispersed in a nematic LC. a, Three-photon excitation fluorescence microscopy images of a platelet in an LC cell, obtained at the cross-sectional plane (x–z plane) passing through the middle of the platelet, and at the vertical plane (x–y plane) that is orthogonal to the plane of the cell and the large-area faces of the platelet. Both planes pass through the centre of mass of the particle. **b**, Scanning electron microscopy image of an individual platelet placed on a substrate. **c**, Schematic of a platelet suspended in a nematic LC. Green rods indicate the director field $\boldsymbol{n}(\boldsymbol{r})$; red rods indicate the orientation of the azobenzene molecules on the surface of the platelet; the black semi-sphere on one of the vertices of the hexagon represents the surface point defects called 'boojums'. The optical torque that rotates the platelet away from its equilibrium state is balanced by the counteracting elastic torque caused by director twisting, as shown by the blue and red curved arrows.

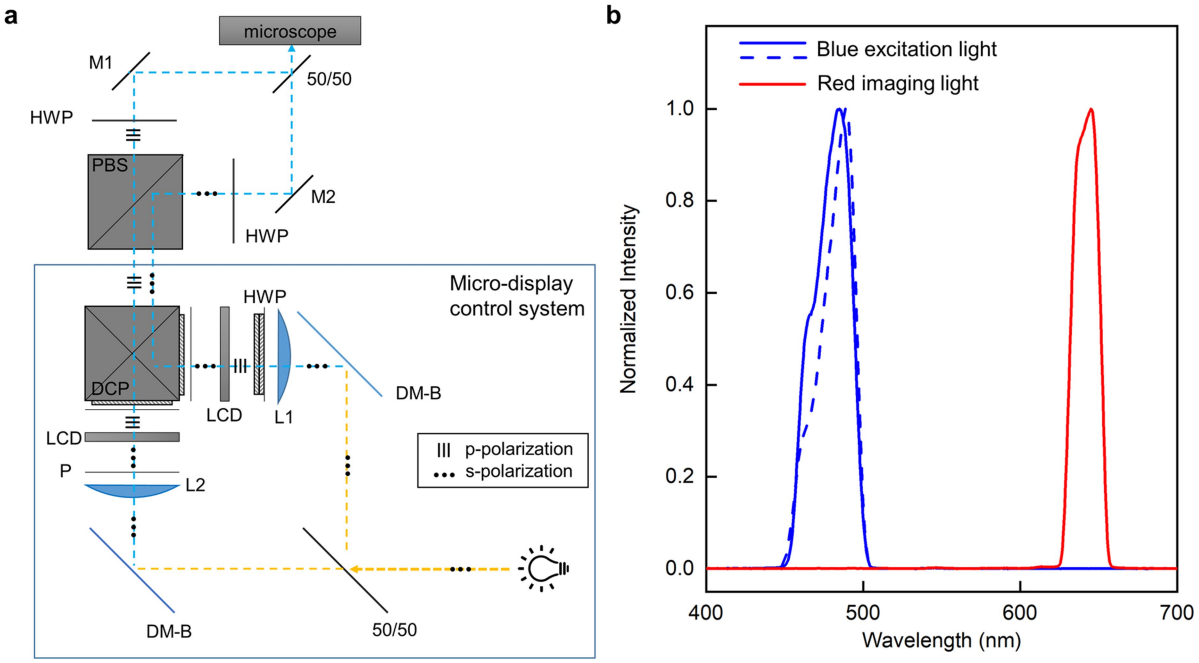

Extended Data Fig. 2 | Microdisplay-based illumination control system setup. a, Schematic of the optical illumination setup. White light from the lamp is split in half and directed into two optical paths using a beam splitter, filtered by two separate dichroic mirrors to supply blue light to two of the LC microdisplays (LCDs). After passing through the microdisplays, which define the spatial patterns of illumination, the two light beams are recombined by a dichroic prism and then separated again on the basis of their polarization. The two separated light paths correspond to patterns generated on the two LCDs and their polarization is further controlled by the half-wave plates. Additional mirrors enable fine-tuning of the position of the projected patterns after the light is re-combined and coupled into the microscope. In the schematic, '50/50' denotes the plate beam splitters (BSW10R, Thorlabs); 'DM-B' indicates the dichroic mirrors that reflect blue light; L1 and L2 are convex lenses; 'HWP' denotes half-wave plates; 'P' represents the polarizer; 'DCP' is a dichroic cross-prism; 'PBS' is a cube polarizing beam splitter (CCM1-PB251, Thorlabs); M1 and M2 are silver mirrors. **b**, Spectra of the red imaging light obtained by filtering the light of the microscope lamp, and of the blue excitation light from the microdisplay control system. Solid and dashed blue lines are the spectra of the two blue channels when turned on separately.

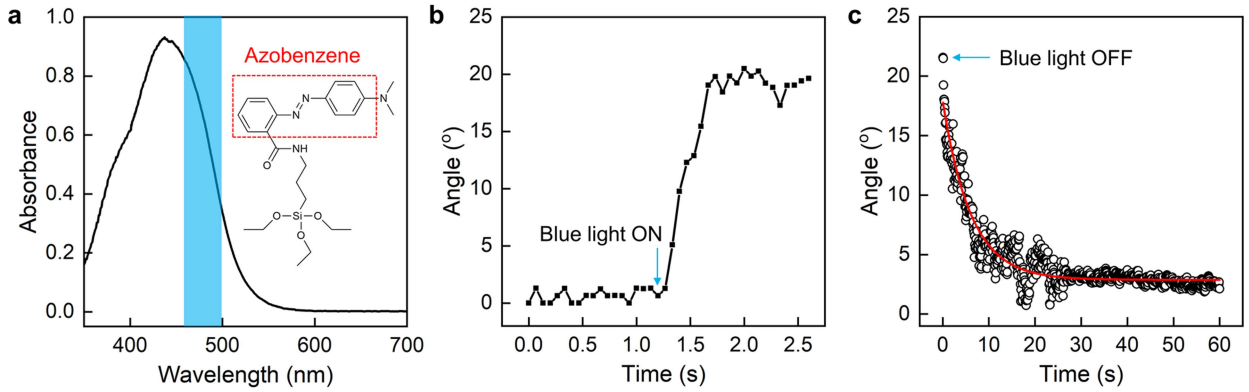

Extended Data Fig. 3 | Optical response of azobenzene-containing molecules and monopole-like platelets in a nematic LC. a, Absorbance spectrum of the photosensitive molecules of derivative methyl red in toluene at a concentration of 5×10^{-5} M. The spectrum was obtained using a 1-cm-thick cuvette with a spectrometer (Cary 500, Varian). **b**, Time dependence of the azimuthal orientation angle of the platelet upon switching on the blue excitation light at time $t \approx 1.2$ s, showing how the monopole moment is turned on upon light exposure. **c**, Time dependence of the azimuthal orientation angle of the platelet relative to its equilibrium position upon switching off the blue excitation light at $t = 0$ s.

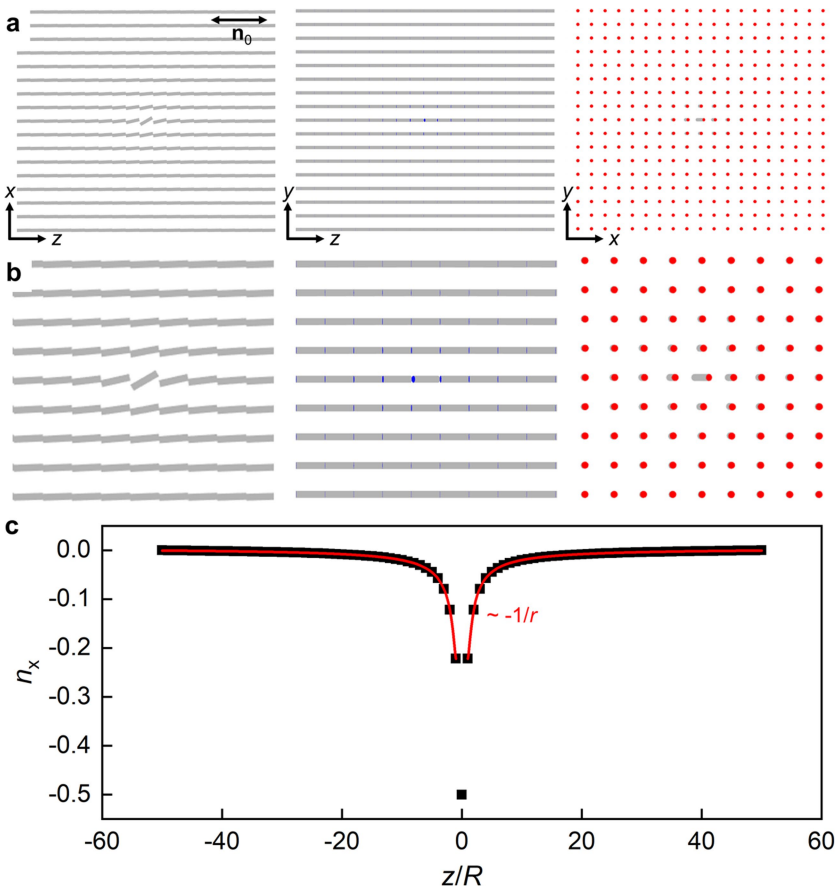

Extended Data Fig. 4 | Computer simulated director configuration of an elastic monopole. a, Cross-sections of the director structure in the *x*–*z*, *y*–*z* and *x*–*y* planes passing through the centre of the structure. The local director orientation is shown by grey cylinders with blue and red ends. **b**, Zoomed-in view of the cross-sections shown in **a**. **c**, Distance dependence of the director deviation n_x along the *z* axis. The simulated results (black squares) are fitted with the function $n_x \propto -1/r$ anticipated for monopoles (red lines). *R* represents the effective particle size.

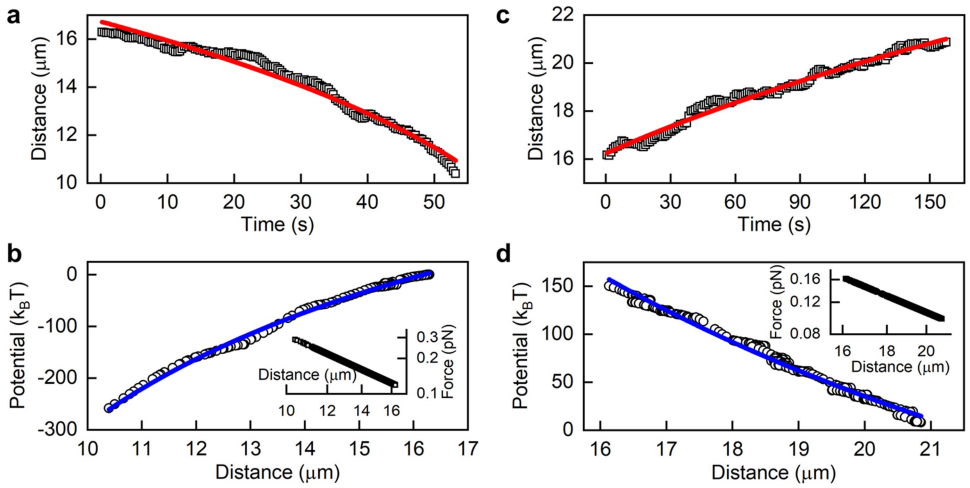

Extended Data Fig. 5 | Characterization of interactions between elastic monopoles. The strength of the elastic monopoles considered here differs from that in the main-text figures. **a**, **c**, Separation distance versus time of monopolar attraction (**a**) and repulsion (**c**). Red lines in **a** and **c** are the best fits of the experimental data with the function $r_c(t) = (r_0^3 - 3\alpha t)^{1/3}$ and with fitting coefficients $r_0 = 16.7\,\mu m$, $\alpha = 21.1\,\mu m^3\,s^{-1}$ (**a**) and $r_0 = 16.2\,\mu m$, $\alpha = -10.6\,\mu m^3\,s^{-1}$ (**c**). **b**, **d**, Dependence of the corresponding potential and force (insets) on the distance. Blue lines are the best fits of the experimental data with a potential proportional to $\pm 1/r_c$. The elastic charge estimated from the fitting parameters is 0.51 μm (**a**, **b**) and 0.36 μm (**c**, **d**).

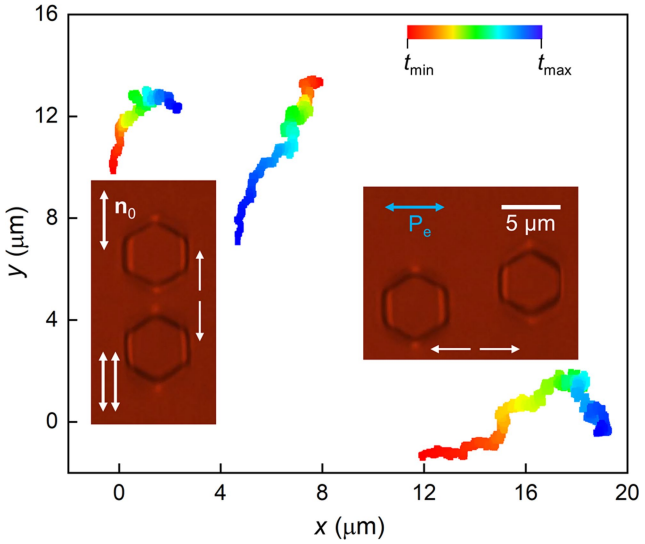

Extended Data Fig. 6 | Angular dependence of quadrupolar interactions. Trajectories are colour-coded with the time elapsed since the release of the platelets from the laser traps, and the duration of interaction is $t_{max} - t_{min} \approx 100$ s. The insets are micrographs of platelets repelling each other when the separation vector that points from the centre of one particle to that of the other is roughly parallel or perpendicular to $\boldsymbol{n}_0$. The images were taken using parallel polarizers shown by the white double arrows. By contrast, the platelets attract when the separation vector is at an angle with respect to $\boldsymbol{n}_0$, as shown by the trajectory in the middle; the corresponding distance-versus-time dependence is shown in Fig. 4e.

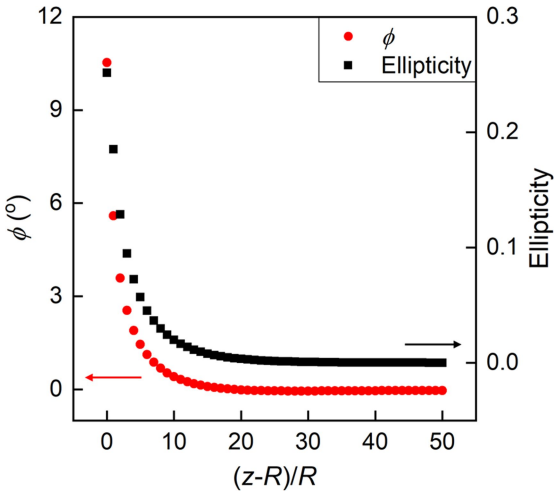

Extended Data Fig. 7 | Computer-simulated polarization states of the red imaging light after passing through the sample. The angle ϕ between the long axis of the polarization ellipse and $\boldsymbol{n}_0$ and the corresponding ellipticity are shown with red dots and black squares, respectively. The horizontal axis $(z - R)/R$ represents the distance from the edge of the particle along the z direction relative to the particle radius R.